Title

Rapid Determination of Near-Fault Earthquake Deformation Using Differential LiDAR

Journal

Bulletin of the Seismological Society of America, 102(4)

Authors

Borsa, Adrian Antal
Minster, Jean Bernard

Publication Date

2012-08-01

Rapid Determination of Near-Fault Earthquake Deformation Using Differential LiDAR

Adrian Borsa[1], Jean-Bernard Minster[1]

[1]Scripps Institution of Oceanography

University of California, San Diego

9500 Gilman Drive, Mailstop 0225

Abstract

Improved near-field measurements of earthquake slip and deformation patterns have the potential for expanding our understanding of fault behavior and the relationship of active faulting to topography. Current techniques for obtaining these measurements – including field observation, GNSS displacement estimation, and optical or radar remote sensing – have limitations that can be mitigated by the inclusion of results from differential airborne LiDAR analysis of the rupture zone. The 2005 airborne LiDAR survey of the southern San Andreas, San Jacinto and Banning faults (the "B4 survey") mapped 1100 km of the most seismically active fault systems in southern California for the purpose of providing a baseline for determining slip from a future earthquake. We used the B4 survey to develop a processing algorithm that yields rapid estimates of near-fault ground deformation using simultaneous cross correlation of both topography and backscatter intensity from pre-earthquake and simulated post-earthquake LiDAR datasets. We show robust recovery of the direction and magnitude of an applied synthetic slip of 5 m in the horizontal and 0.5 m in the vertical within our area of study, with clear discrimination between areas with and without applied slip. We also successfully recovered more complex deformation from a modeled fault stepover in the same study area. Our results indicate that we should be able to recover slip to accuracies of better than 20 cm in the horizontal and 1 cm in the vertical, at a spatial resolution of ≤15 m for LiDAR datasets with sample densities as low as 0.5 points/m^2.

Introduction

Despite the burgeoning deployment of new geodetic technologies capable of measuring ground displacements on a variety of spatial and temporal scales, obtaining a comprehensive picture of surface deformation and slip in the near-field of an earthquake remains a challenge.

Better near-field measurements could substantially improve our understanding of several outstanding problems in tectonic geophysics, including the source of the shallow slip deficit observed for surface-rupturing earthquakes such as Landers (Fialko, 2004), Hector Mine (Simons et al., 2002) and Izmit (Cakir et al., 2003). Interferometric Synthetic Aperture Radar (InSAR)-derived displacement fields for these surface-rupturing earthquakes typically do not extend close enough to the rupture zone to fully characterize displacement gradients within a few km of the fault. These gradients are needed to map the extent of the compliant damage zone implicated in producing the shallow slip deficit (Fialko et al., 2005; Barbot et al., 2008). Another area of research that would benefit from synoptic-scale mapping of near-field deformation from large earthquakes is the correlation of the surface expression of individual events with pre-existing tectonic landforms. Some studies of recent earthquakes (Pucci et al., 2006) have demonstrated a divergence between the impacts of single and cumulative events on topography, providing evidence for the long-term evolution of these fault systems. Others (Lin et al., 2001; Lin et al., 2011) indicate very close alignment between coseismic displacements and pre-existing structures. Improving the sampling density and spatial extent of both topography and superimposed displacements would facilitate a more quantitative approach to this problem for future earthquakes.

Global Navigation Satellite Systems (GNSS) and Global Positioning System (GPS) techniques are capable of sub-centimeter measurements of coseismic surface displacement over broad areas (Wdowinski et al., 1997; Ozawa et al., 2004), but even the 1100-station Plate Boundary Observatory GPS network has a spatial resolution of only 10~20 kilometers in its areas of densest coverage. InSAR offers sub-decimeter accuracy, broad areal coverage and sub-kilometer spatial resolution (Figure 1), but requires at least two pairs of images to adequately resolve all components of surface displacement. The need for multiple image pairs exacerbates InSAR's problem with decorrelation in the near-field of a rupture (Fialko et al., 2001), since the

combined interferogram is only valid in areas where all of its constituents yield valid displacement estimates. Attempts to address this problem have led to the use of cross-correlation of SAR amplitude images to yield estimates of coseismic displacements (Michel et al., 1999; Yun et al., 2007). A similar approach has been successfully used on aerial (Michel and Avouac, 2006) and satellite (Michel and Avouac, 2002) pan-chromatic images. Although image cross-correlation yields near-fault measurements at a resolution of hundreds of meters, it is limited to horizontal ground displacement and suffers from reduced performance in areas where the images are of nearly uniform brightness (i.e. are flat).

Even in this era of widely available geodetic remote sensing data, field measurements are still used for measuring slip in the near field of an earthquake. Both vertical and horizontal relative slip can be measured and the methods employed are time-tested, although the resources required for surveying long ruptures and the need to locate unambiguously-offset features limit the sampling density. Intensive fieldwork following the 1999 M 7.1 Hector Mine earthquake resulted in 400 observations over 48 km (Treiman et al., 2002), implying an average sampling interval of about 100 meters along-strike. The 2002 M 7.9 Denali earthquake, which ruptured remote terrain in central Alaska, was characterized by 127 field measurements over 300 km (Haeussler et al., 2004), implying a much lower average sampling resolution of 2 km. And since only the slip directly across identified rupture traces is measured, areas of broad deformation or locations where the fault splays or steps over are likely to be poorly characterized. Field measurements may therefore underestimate total slip across the rupture zone, as was observed in the comparison of field-based slip estimates for the Hector Mine earthquake with extrapolated slip from InSAR measurements in the far-field (Sandwell et al., 2002).

Airborne Light Detection And Ranging (LiDAR) has the capacity to address many of the shortcomings of other methods of measuring earthquake surface deformation. Also known as

airborne laser swath mapping (ALSM), airborne LiDAR techniques use the time of flight of ground-reflected energy from an aircraft-mounted scanning laser to map sub-decimeter surface topography at a spatial resolution of better than 50 cm (Rabine et al., 1996; Slatton et al., 2007). The intensity of backscattered energy is also recorded for each ground return and provides independent information that can be used to characterize surface features. Spatial coverage off the fault is determined by the width of the survey corridor, which typically spans no more than a few kilometers on either side of the fault. LiDAR makes up for its narrow fault-targeted coverage with a combination of superior spatial resolution and its potential for unambiguous determination of all components of surface deformation.

Earthquake slip estimation using LiDAR has been limited to date to the analysis of post-event data acquired months to decades or longer after an earthquake (Hudnut et al., 2002; Zielke et al., 2010). With no pre-event data to provide an absolute reference for subsequent measurements, these studies have focused on measuring localized slip at recognizable rupture traces, where the signal is large and opposing relative motion across the fault results in easy-to-identify offsets in topography. This focus on slip associated with surface-expressed faulting is the same limitation that restricts the effectiveness of field measurements, although post-event LiDAR analysis has an advantage in that it can be used to generate nearly continuous slip estimates along the entire length of the rupture.

The real potential of LiDAR data for earthquake studies can only be realized when pre-event and post-event data are compared to give a synoptic view of coseismic deformation over the entire rupture zone. While this comparison is often referred to as "differencing" the pre- and post-event datasets, it in fact involves finding the 3D displacement field that optimally maps one to the other. In this paper, we present a comparison algorithm that requires no *a priori* specification of fault locations; robustly identifies surface deformation, even in the presence of noise; allows advance processing of the pre-event dataset to speed up execution time when the

post-event dataset becomes available; and supports partitioning of the datasets for parallel processing, which is required for rapid processing of LiDAR datasets that can reach hundreds of millions of points for even a few tens of kilometers of mapped surface rupture. With the probability of a large earthquake occurring on a previously-mapped fault increasing as a result of ongoing airborne LiDAR acquisitions, there is an immediate need to develop and assess such algorithms in anticipation of a rapid post-event LiDAR survey and the opportunity such a dataset would provide for new scientific investigations.

LiDAR Dataset

Over the past decade, there has been extensive collection of airborne LiDAR data along major active faults in California and elsewhere (Prentice et al., 2003; Bevis et al., 2005; Phillips et al., 2008), with several acquisitions occurring after significant earthquakes (e.g. Hector Mine, Denali, El-Major Cucapah). To date, only the El-Mayor Cucapah fault zone has been mapped by airborne LiDAR both before and after a surface-rupturing earthquake, however this dataset is not publicly available. In the absence of pre-event observational data for testing and validating comparison algorithms such as ours, we use data from the "B4" airborne LiDAR survey of the southern San Andreas Fault (Bevis et al., 2005), synthetically slipped to simulate offsets that might result from a surface-rupturing earthquake. The B4 dataset was acquired in 2005 for the express purpose of providing a baseline for post-earthquake slip determination and is thus an ideal testbed for the development of the algorithm we present here.

Our study area lies within an alluvial fan that spans the San Andreas Fault (SAF) about 7 km northwest of Desert Hot Springs, CA (Figure 2). Total topographic relief is 37 m over a distance of about 800 m, three-quarters of which is due to the planar trend of surface from SE to NW. The habitat is desert scrub with canopy cover of less than 50% (estimated from field observations). The generally shallow slopes and sparse vegetation of the study area represent a

near-best-case scenario for the interpretation of LiDAR data, but similar conditions prevail for most of the LiDAR-surveyed faults in Southern California.

For our pre-event dataset, we use the LiDAR point cloud from a single aircraft pass (designated "Str_63" in the survey metadata) over the study area. This point cloud consists of 600,000 individual measurements of topography and infrared backscatter intensity over an area of 320,000 m^2, implying an average sample density of ~2 points per square meter. Because topographic features such as bushes and trees are useful for tracking surface displacements, we use the unclassified "first-return" point cloud associated with the highest reflecting surface in each laser footprint. This point cloud primarily samples the top of all natural and anthropogenic features and does not involve the classification (and, typically, removal) of non-surface returns.

For our post-event dataset, we took the pre-event point cloud and applied a homogeneous synthetic 5 m right-lateral horizontal slip and 0.5 m positive vertical slip on a vertical fault plane roughly aligned with the trace of the SAF, representing a simple case of primary slip concentrated on a single linear fault trace. All of the displacement is confined to the northeast side of the fault (i.e. on the North American Plate), which allows us to use the unslipped southwest portion of the data as an experimental control.

Figure 3a illustrates the detrended elevation and Figure 3b the intensity patterns of this synthetically slipped point cloud, with topography shown relative to the lowest point in the scene and intensity given in arbitrary units scaled from 0 to 255. The line bisecting the image marks the division between slipped points to the NE and unslipped points to the SW, and the wavy boundary of the data region is due to aircraft roll motion shifting the pointing direction of laser in the across-track direction. Channels in the alluvial fan are apparent in the topography, as are the shallow valley containing the main N-S trending stream channels, a SE-NW trending paved road and an E-W trending dirt road. The intensity image is much "flatter" overall, but it emphasizes some smaller-scale details that are not as obvious in the topography.

LiDAR Cross-Correlation Technique

Spatial cross-correlation techniques have been successfully adapted to problems that involve comparing before and after topography datasets similar to those we are examining in this study. Duffy and Hughes-Clarke (2005) used cross-correlation to map the horizontal migration of seafloor dunes using bathymetry data, as did Kääb and Vollmer (2000) to estimate the horizontal and vertical motion of a rock glacier using photogrammetry data. Both studies investigated surface changes without invoking *a priori* assumptions about the nature of those changes, as we wish to do here. Although *a priori* information about the localization of earthquake slip along surface ruptures is often available from aerial photography soon after an event, we do not want our algorithm to rely on this information but rather to quickly generate it for use by other researchers. This is particularly important where surface deformation may not be accompanied by visible faulting, such as at blind thrust faults, near the ends of a strike-slip rupture, at fault step-over locations, or where slip is distributed across multiple fault strands.

In this study, we employ a local cross-correlation technique that maximizes correlation between small overlapping areas of two datasets to generate the displacement vector between them, conceptually similar to the techniques used in the studies cited above. One difference in our approach is that we do not rely on a regular search of the parameter space to determine displacements, but instead employ an iterative least-squares inversion to increase execution speed. Each correlation calculation is performed independently, so displacements that are consistent across multiple adjacent areas are less likely to be artifacts of the calculation than would be the case if external constraints were applied. We do not estimate rotations or strain between the pre and post-event data, assuming that any slip or deformation can be described by rigid translations at the scale of our analysis. This assumption did not appear to impact algorithm

performance except where deformation gradients were high, such as directly across the fault rupture plane.

We note that the Iterative Closest Point (ICP) technique, originally developed to solve problems of surface and point registration in the field of machine controls (Besl, and McKay, 1992; Trucco et al., 1999), is an alternative to cross-correlation for solving the problem posed here. One limitation of ICP-style algorithms is that since they require full-resolution point clouds or similar-resolution derivative products as inputs, pre-processing to simplify the pre-event point cloud for later analysis is not an option for reducing processing times. In addition, our experience using one variant of the ICP algorithm (icp.m, written by Per Bergstrom) is that it was about an order of magnitude slower than our algorithm (even without pre-processing) and that it yielded noisy results that tended to underestimate imposed slip. Our naïve implementation of ICP is probably underestimating its true potential for this application, however.

Step 1: Modeling the LiDAR Point Cloud

While the problem of cross-correlating two LiDAR point clouds is analogous to that of cross-correlating images or digital elevation models (DEMs), point clouds consist of arbitrarily-distributed point measurements that typically do not overlie each other and thus cannot be directly differenced to calculate a correlation metric. A common way to simplify the cross-correlation calculation is to grid the point cloud data and run the cross-correlation algorithm directly on the resulting DEMs. But even if the DEM resolution is properly chosen and a reasonable autocorrelation relationship is assumed when filtering the data, the drawback to this approach is that the DEM (which is missing information contained in the original point cloud) must be reinterpreted to provide topographic gradient and curvature information that could more accurately be extracted from the point cloud itself. In addition, if the underlying surface

represented by a point cloud can be simply modeled as we do below, a DEM is an inefficient way to characterize that surface.

Instead of creating a DEM from the point cloud, we generate a smoothed surface model H (Figure 4, top) by fitting point elevations with a set of basis functions that can be analytically differentiated and whose coefficients provide quick access to the underlying topography and topographic gradients. In our implementation, we fit the pre-event point cloud with the 2-D harmonic basis set described by (James, 1966)

$$H(x,y) = \sum_{k=0}^{m} \sum_{l=0}^{n} a_{k,l} \left[\sin\left(\frac{2\pi x}{L_x} k \right) + i \cos\left(\frac{2\pi x}{L_x} l \right) \right] \left[\sin\left(\frac{2\pi y}{L_y} k \right) + i \cos\left(\frac{2\pi y}{L_y} l \right) \right]. \quad (1)$$

where x and y are the UTM coordinates of the data, L is the size of the fitting region in the x and y coordinate directions, the number of terms in the basis set is set by m and n, and the complex-valued coefficients $a_{k,l}$ are found via least squares fitting. To ensure that the fit resolution is identical in both coordinate directions, we set $L_x = L_y$ and $m = n$. We always take L to be twice the span of the data in order to handle edge effects related to the periodic extension of the fitting window in the plane. Since the autocorrelation assumed by harmonic fitting is sinusoidal, this choice of L also means that the autocorrelation function for the order-1 harmonics is that of a cosine window over the extent of the data, which adequately captures the long-wavelength topography in the point cloud.

LiDAR point clouds also contain information about the intensity of ground-reflected energy from the laser footprint (Figure 3b). Although intensity measurements are somewhat noisy, they are spatially coherent and can complement elevations in the determination of slip, especially in areas where the topography is flat. We fit point cloud intensities exactly as we do elevations in Equation (1), yielding the intensity model $B(x, y)$. Both $B(x, y)$ and $H(x, y)$ can be

calculated for pre-event datasets in advance of collection of the post-event dataset, reducing the time required for differential analysis when the second point cloud finally becomes available.

Step 2: Cross-Correlating Pre- and Post-Event Datasets

To perform the cross-correlation step of our algorithm, we subdivide the area covered by the post-event point cloud into individual square pixels of edge length S and step pixel-by-pixel through the entire region for which we have overlapping pre- and post-event data. It is not necessary to model the post-event point cloud to cross-correlate it with the pre-event dataset. Instead, the N points (x_i, y_i, z_i, b_i) within each pixel of the post-event dataset (b denotes the intensity/brightness measurement) are compared directly to the continuous functions $B(x, y)$ and $H(x, y)$ to estimate the displacement vector $\mathbf{x} = <\Delta x, \Delta y, \Delta z>$ that simultaneously minimizes the chi-square elevation and intensity misfits between them (Figure 4, bottom).

Written as a generalized least squares problem, we are trying to find the $\mathbf{x}$ that minimizes the functional

$$f(\Delta x,\Delta y,\Delta z) = \sum_{i=1}^{N}\left\{\frac{\left[H(x_i+\Delta x, y_i+\Delta y)+\Delta z\right]-z_i}{\sigma_{z_i}}\right\}^2 \quad (\text{topography}) + \lambda\sum_{i=1}^{N}\left\{\frac{\left[B(x_i+\Delta x, y_i+\Delta y)\right]-b_i}{\sigma_{b_i}}\right\}^2 \quad (\text{intensity}) \tag{2}$$

where λ is a user-selected parameter that determines the relative weights of topography and intensity in the inversion and the σ are the standard errors on elevation and intensity for each point i. $\mathbf{x}$ is determined independently for each pixel, which means the algorithm is not guided by an *a priori* slip model. While this may increase variability in the recovered displacement field between the pre- and post-event datasets, it also makes the algorithm much more useful in situations where slip or deformation is unknown. We also note that because of the typical

variability in intensity values between airborne LiDAR surveys due to aircraft flying height and other effects, the post-event point intensities b_i in Equation (2) are normalized to have the same mean as that of the pre-event intensity model B within each comparison pixel.

Because B and H are functions of the solution $\mathbf{x}$, Equation (2) is non-linear and must be solved iteratively. For each comparison pixel in our region of interest, we solve for $\mathbf{x}$ using the Gauss-Newton algorithm described by

$$\begin{aligned} &\left[\mathbf{J}\left(\mathbf{x}^k\right)^T \mathbf{J}\left(\mathbf{x}^k\right)\right]\mathbf{x} = -\mathbf{J}\left(\mathbf{x}^k\right)^T \mathbf{F}\left(\mathbf{x}^k\right) \\ &\mathbf{x}^{k+1} = \mathbf{x}^k + \mathbf{x} \\ &k = k+1 \end{aligned} \tag{3}$$

where $\mathbf{F}(\mathbf{x})$ is the matrix of pre- and post-event data misfits

$$\mathbf{F}(\mathbf{x}) = \begin{bmatrix} \left\{\left[H\left(x_1+\Delta x, y_1+\Delta y\right)+\Delta z\right]-z_1\right\}/\sigma_{z_1} \\ \vdots \\ \left\{\left[H\left(x_N+\Delta x, y_N+\Delta y\right)+\Delta z\right]-z_N\right\}/\sigma_{z_N} \\ \left\{B\left(x_1+\Delta x, y_1+\Delta y\right)-b_1\right\}/\sigma_{b_1} \\ \vdots \\ \left\{B\left(x_N+\Delta x, y_N+\Delta y\right)-b_N\right\}/\sigma_{b_N} \end{bmatrix} \tag{4}$$

$\mathbf{J}(\mathbf{x})$ is the Jacobian matrix of the first partial derivatives of $\mathbf{F}(\mathbf{x})$

$$\mathbf{J}(\mathbf{x}) = \left[\frac{\partial \mathbf{F}(\mathbf{x})}{\partial \Delta x} \quad \frac{\partial \mathbf{F}(\mathbf{x})}{\partial \Delta y} \quad \frac{\partial \mathbf{F}(\mathbf{x})}{\partial \Delta z}\right] \tag{5}$$

and we allow the algorithm to fully update $\mathbf{x}^{k+1}$ in each step (the incremental increase in $\mathbf{x}^{k+1}$ can be damped by a factor $\alpha < 1$ where $\mathbf{x}^{k+1} = \mathbf{x}^k + \alpha\mathbf{x}$, but we did not find this to be necessary to ensure convergence). Empirically, we found the Gauss-Newton solution to be 2+ orders of magnitude faster than an incremental search of the likely parameter space at a resolution of 10

cm in the horizontal and 1 cm in the vertical, which makes the grid search approach prohibitively expensive in most cases.

We can vary three parameters to tune the performance of the algorithm: the size S of the comparison pixel, the relative weighting λ between topography and intensity in the inversion, and the resolution length scale of pre-event data models $B(x, y)$ and $H(x, y)$ as determined by L, m and n. In order to understand the impact of these choices on processing speed and the fidelity of the recovered displacement vector field $\mathbf{x}(x, y)$ relative to the known applied synthetic slip model, we ran multiple realizations of the algorithm for the same input data. We describe our findings in the Results and Discussion section below.

One caveat to this study is that we did not attempt to model the effect of data error on the accuracy of the cross-correlation. Point-cloud data are the output of a multi-step geolocation process, which is subject to calibration error that can obscure or mimic the topographic change signal of interest (Borsa et al., 2007). In addition to geolocation errors, different reference frames between two surveys would introduce a systematic offset that could be mistaken for coseismic displacements, especially if only a small area is being investigated. While the differences between recent versions of the ITRF (International Terrestrial Reference Frame) are only at the cm level, the magnitude of reference frame error exceeds 1 meter between NAD83 and the ITRF, underscoring the need for maintaining and paying attention to reference frame metadata for LiDAR data collections. Our results should therefore be considered to be best-case, with further work needed to determine the potential impact of geolocation accuracy.

We also note that the Gauss-Newton inversion method requires that the initial value of the solution be located where the downhill gradient of the misfit manifold leads to the global minimum defined by the actual solution. In cases where the amplitudes of shorter-wavelength constituents in the topography/intensity models rival those of longer-wavelength constituents, it is likely that our correlation method would not work unless the initial solution was close to the

correct solution. Other approaches such as simulated annealing would be much more likely to succeed in these cases, albeit at the cost of much longer execution times.

Results and Discussion

An Initial Displacement Solution for Synthetically Slipped Data

Figure 5a shows the horizontal and Figure 5b the vertical components of the displacement field $\mathbf{x}(x, y)$ we obtained by applying our algorithm to the synthetically slipped data in Figure 3. Total processing time for our 2.5 km^2 study area was 8 minutes on a single-processor computer. We did not try to optimize the solution for speed or accuracy, but used nominal values for the three user-selectable parameters (a pixel size S of 15.0 m, a topography/intensity weighting factor λ of 1.0, and a model fit resolution of 12.5 m) and assumed zero initial slip in each pixel, which meant that the solution vector started off quite far from its true value within the slipped region. Even without tuning any parameters, the algorithm was successful in recovering most of the imposed synthetic slip, while indicating little or no slip in the control region. Qualitatively, 1.) there is a clear delineation between the control region below the slip plane and the slipped region above, 2.) recovered vectors in the slip region exhibit strong correlation in both magnitude and direction, and 3.) anomalous vectors do not impact the overall interpretation of where slip has and has not occurred.

Although the fidelity of the solution is particularly good in the zero-slip control region, the displacement field in the slipped region is less accurate, with a number of horizontal vectors pointing in the wrong direction and inconsistency in the magnitudes of the vertical vectors. The fact that the algorithm's poorer performance was confined to the slipped region suggests that the zero initial value of the slip vector can lead to sub-optimal solutions for pixels with large offsets between pre-event and post-event surfaces. This is in fact what we found when we investigated

the convergence of the solution in pixels with large misfits between expected and recovered offsets: while the misfit manifold exhibited a deep minimum around the value of the true slip, there was also a local (erroneous) secondary minimum in the "downhill" direction from zero to which the inversion was converging.

Improving the Displacement Solution

In order to improve the fidelity of the recovered slip field, albeit at the cost of roughly doubling processing time, we reran the algorithm using the solution from Figure 5 to initialize the displacement field. Specifically, we averaged the displacement solution within a radius of 4*S* to provide a starting vector for each pixel and ran the inversion exactly as before. Figure 6 shows the recovered displacement field from this second run of the algorithm, and Figure 7 summarizes the misfit between this recovered field and the known synthetic field we are trying to reproduce. While the result in the control area is little changed, the recovery of the displacement field in the slipped region is noticeably improved. The spatial plots at the left of Figure 7 show equally small misfits in both the control and slipped regions, with a few larger-magnitude misfits apparent along the data discontinuities represented by the boundary between slipped/unslipped data and to a lesser extent by the road running through the control region (the dark blue line in the Figure 3b intensity plot). This result is mirrored in the histograms of horizontal and vertical magnitude misfits at the right of Figure 7 and in the statistics of the misfit distributions (first column of Table 1), both of which reveal similarly accurate results in the slipped and control regions. Specifically, the magnitude misfit between the imposed and recovered displacement vectors in the slipped region is 17.1 ± 17.7 cm (median ± IQR) for the horizontal and 0.5 ± 0.7 cm for the vertical, which is comparable to the control region values of 18.5 ± 17.9 cm and 0.6 ± 0.9 cm, respectively.

The recovery of the azimuth of the imposed synthetic slip is also very good. In the slipped region, the azimuth misfit histogram is zero-mean and narrow (0.0 ± 1.9 degrees), reflecting a high degree of fidelity in the recovery of the imposed slip. In the control region, the flat control-region histogram (-1.5 ± 181 degrees) is consistent with zero-slip conditions: since the azimuth of a zero-length vector is undefined, the algorithm correctly returns directions that are uniformly distributed across 360 degrees. This accounts for the large azimuthal IQR, relative to which the slightly negative mean misfit is insignificant. We note that we achieved almost identical azimuth/magnitude accuracy when we ran the algorithm on data with half the imposed slip (2.5 m horizontal and 0.25 m vertical), indicating that algorithm accuracy is independent of the magnitude of ground displacements, at least within the range of values of interest.

Overall, these results show that 1.) misfits in the slipped region exhibit minimal bias and variance relative to the imposed *a priori* displacement, and 2.) misfits in the control region are consistent with low-level random noise in the fitting algorithm and no systematic effects. For the purpose of constraining earthquake slip inversions or providing near-field control on fault slip for moderate-to-large magnitude earthquakes, this level of performance is more than sufficient.

Resolution and Accuracy Limits of the Algorithm

In order to understand how the choice of algorithm parameters impacts solution accuracy, we examined the effects of varying the comparison pixel size, model resolution and topography/intensity weighting over a range of plausible values. Figure 8 summarizes these results, showing the median misfit of the estimated displacement field in the slipped (top) and control (bottom) regions of the dataset for 120 different combinations of these parameters. Specifically, we varied pixel size in 2.5 m increments from 7.5 m and 15.0 m, grouping the misfit results for each value of *S* from left to right in Figure 8. The different shades within each pixel-size group represent stepwise changes in the resolution of the pre-event point cloud model,

from 50.0 m (leftmost circles) to 25.0 m, 16.7 m, 12.5 m and 10.0 m (rightmost circles). Finally, within each resolution grouping, the plotted points from left to right correspond to λ values of 0.0, 0.5, 1.0, 1.5, 2.0 and 2.5.

The results of this analysis show that the relative weighting of topography and intensity in the algorithm has an impact on solution accuracy only when intensity is ignored ($\lambda = 0.0$) or underweighted ($\lambda = 0.5$). Equal weighting of topography and intensity ($\lambda = 1.0$), while not always yielding the absolute lowest misfit, gives nearly the lowest misfit for the entire range of other parameters and represents a good default value to use for this dataset. Higher values of λ neither improve nor degrade the solutions significantly for our test dataset.

Increasing the fit resolution of the harmonic model increases variability in the model, which improves the precision of the pixel-by-pixel inversions while also raising the likelihood of local minima in the solution manifold. The result is generally improved solution accuracy as resolution steps from 50.0 m to 10.0 m, with the caveat that this relationship can break down for higher values of fit resolution unless the algorithm is run twice (like we do in our second example above). Improved accuracy comes at the price of execution speed. Each increase of fit resolution – achieved by incrementing the values of *m* and *n* in the harmonic fit to the pre-event point cloud data – yields a 30~60% reduction in horizontal/vertical magnitude misfit while doubling the time required to run the algorithm.

Finally, the effect of increasing pixel size is improved accuracy for solutions calculated using any combination of values of the other parameters. The improvement in misfit for each 2.5 m increase in pixel size is about 20~40%, with less impact as the pixel size approaches 15.0 m. In addition, algorithm execution time varies by the inverse square of pixel edge length *S*, which results in a fourfold increase of speed going from 7.5 m to 15 m pixels. The first two columns of Table 1 show how the misfit statistics for the example in Figure 6 are impacted by reducing pixel size from 15 m to 10 m. While the median misfit of the recovered azimuths is still zero, the

median horizontal and vertical magnitude misfits have roughly doubled, to 1 cm and 40 cm respectively. Nevertheless, in cases where recovering the greatest possible spatial detail in the slip field is paramount, smaller values of *S* can be used despite the loss of accuracy and speed.

We also experimented with decimating the dataset at various levels to see how lower point cloud densities might affect the solution. Our original dataset had a mean spatial density of 2 points/m^2. We successively decimated the dataset by factors of 2 and reran the solution for the example shown in Figure 6 each time. Columns 1, 4 and 5 of Table 1 show that the solution is negligibly impacted by decimating the input data down to 0.5 points/m^2. Beyond this limit, decimation begins to impact the quality of the solution, as expected given the fact that the increasing Nyquist wavelength of the sampling introduces commensurately greater aliasing of short-wavelength topography and intensity. While our assumption of spatially homogeneous slip within each comparison pixel allows us to leverage all intra-pixel data toward a single robust estimate of slip, for best performance we require that LiDAR datasets be collected at sufficient shot density to characterize all but a few percent of surface variance. This is true even though we use low-order (and thus long-wavelength) harmonic basis functions to model the pre-event data: the point cloud has to sufficiently sample the underlying topography/intensity to avoid biasing the harmonic model.

The best overall solution we obtained in this experiment (see Table 1, column 3) had a pixel size of 15.0 m, model fit resolution of 10.0 m and a λ of 1.5. While this is consistent with the general patterns we discuss above, what is important to note is that the difference between this solution and others with smaller pixel size (increased spatial resolution), lower model resolutions (faster execution time) and/or different values of λ may not be significant for many applications. Most importantly, the algorithm is robust relative to its operational parameters, yielding good results even when the parameter choices are not optimal.

Testing the Algorithm Against a More Complex Displacement Field

To test the ability of the algorithm to recover more complicated deformation patterns, we prepared a second post-event dataset reflecting deformation from a stepover between two successive fault segments. For this second example, we used the Coulomb 3.2 software package (Toda et al., 2005; Lin, and Stein, 2004) to model the 3D displacement resulting from a 150-meter stepover between two strike-slip faults extending from the surface to 10 km depth in an infinite elastic half-space, each subject to 1 m right-lateral slip equally distributed on both sides of the rupture plane. We translated each point in the pre-event point cloud by the Coulomb-modeled displacements to generate the post-event dataset, whose topography and intensity appears similar to that shown in Figure 3 at this level of magnification.

To obtain our solution, we ran the algorithm using parameters from in the third column of Table 1 and achieved comparable results to those obtained for the slipped region in the simple uniform-slip case: an azimuth misfit of -0.1 ± 7.2 degrees, horizontal magnitude misfit of 11.1 ± 10.5 cm, and vertical magnitude misfit of 0.0 ± 0.7 cm. As shown in Figure 9, we do not have a control region in this example since the entire study area is deformed in some way by the fault stepover. The recovered slip shows the expected pattern of greatest horizontal slip at the north and south of the study area (where the movement on both fault strands is oriented in the same direction) and clearly resolves the horizontal slip gradients associated with the ends of the fault segments. The least horizontal slip occurs in the stepover region, which is where the greatest vertical movement is seen. The slumping in this region is only a few decimeters in magnitude and is the same effect that creates sag ponds between fault stepovers on actual faults. To be able to resolve slip gradients and vertical signals of these magnitudes indicates that differential LiDAR has the potential to identify a broad range of subtle features related to faulting, not just large-magnitude offsets on the main fault strand.

Conclusions

The development of the algorithm we have just discussed was originally motivated by the wish to quickly provide to first responders (in both the emergency services and research communities) the approximate spatial distribution and magnitude of ground deformation from a large earthquake following the expected collection of airborne LiDAR data along a previously mapped fault. Speed was our primary concern, and we planned to realize significant time savings by performing in advance the expensive step of modeling the pre-event point cloud. For the example we showed in Figure 6, this would reduce processing time on a single-processor desktop computer from 8 minutes to 1 minute, which would then make it feasible to run the algorithm for a 100-km long rupture zone in a matter of hours.

Until we carried out this study, we were unaware that the accuracy and spatial resolution of this algorithm could also make it a useful tool for detailed study of coseismic deformation in the near-field of an earthquake. Our results indicate that slip recovery is independent of the imposed slip and suggest that the lower limit of slip detection using this algorithm is 0.1 m in the horizontal and 0.5 cm in the vertical. Even when algorithm parameters are not optimized, which will almost certainly be the case when the *a priori* slip/deformation is unknown, we have identified generally optimal parameter choices for maximizing solution accuracy that should yield robust identification of ground displacements on the order of 0.2~0.3 m in the horizontal and 1~2 cm in the vertical. This sensitivity approaches that of techniques such as InSAR, but at far greater spatial resolution and with less risk of decorrelation.

Finally, while we have discussed the application of this algorithm to the problem of identifying surface deformation imaged by two successive LiDAR surveys of the same terrain, the algorithm is also suitable for performing quality control of data collected during a single survey. All airborne LiDAR surveys are designed to incorporate overlap of up to 50% between

the ground returns from successive flightlines. Any errors in geolocating the survey data will result in inconsistent elevation estimates for these overlapping areas. A comparison of overlapping ground returns for the B4 project data used in this paper revealed that the spatial pattern of the misfit is correlated over long distances and varies with surface topography, aircraft attitude and other variables (Borsa, Bevis et al. 2007). Our algorithm can identify the spatial pattern of the geolocation misfit for all overlapping data in a survey, giving a synoptic view of survey quality that is impossible to achieve with point comparisons between the survey data and arbitrarily distributed ground reference locations. A future paper will examine the potential of our algorithm for improving LiDAR calibration and validation.

Data and Resources

The LiDAR data used in this research are available online from the NSF's OpenTopography Facility (http://www.opentopography.org/). We used ascii-format point cloud data requested via the "B4 Project" link on the Point Cloud page of the OpenTopo website in April 2011. The processing algorithms were coded in IDL and are the authors' own work. They are available upon request.

Acknowledgements

This research was funded by the USGS's National Earthquake Hazards Reduction Program (NEHRP), grant #07HQGR0023. The B4 LiDAR Project collected LiDAR point cloud data of the southern San Andreas and San Jacinto Faults in southern California. Data acquisition and processing were performed by the National Center for Airborne Laser Mapping (NCALM) in partnership with the USGS and Ohio State University through funding from the EAR Geophysics program at the National Science Foundation (NSF). Optech International contributed the ALTM3100 laser scanner system. UNAVCO and SCIGN assisted in GPS ground control and continuous high rate GPS data acquisition. A group of volunteers from USGS, UCSD, UCLA, Caltech and private industry, as well as gracious landowners along the fault zones, also made the project possible**.** We would also like to thank Ken Hudnut at the USGS for providing the research community with LiDAR point cloud data for the B4 survey prior to its current availability from the NSF's OpenTopography Facility. Finally, we wish to thank reviewers Ramon Arrowsmith and Ryan Gold for their insight and feedback, which resulted in key improvements to this manuscript.

References

Barbot, S., Y. Fialko, and D. Sandwell (2008). Effect of a compliant fault zone on the inferred earthquake slip distribution, *Journal of Geophysical Research*, **113**, B06404.

Besl, P. J., and N. D. McKay (1992). A Method for Registration of 3-D Shapes, *IEEE Transactions on Pattern Analysis and Machine Intelligence*, **14**, 2, p. 239–256.

Bevis, M., K. Hudnut, R. Sanchez, C. Toth, D. Grejner-Brezezinska, E. Kendrick, D. Caccamise, D. Raleigh, H. Zhou, S. Shan, W. Shindle, A. Yong, J. Harvey, A. Borsa, et al. (2005). The B4 Project: Scanning the San Andreas and San Jacinto Fault Zones, *Eos Trans. AGU*, **86**, 52, p. H34B–01.

Borsa, A. A., M. Bevis, and K. W. Hudnut (2007). Survey-scale airborne lidar error analysis from parallel swath comparison, *Eos Transactions AGU*, **88**, 52, p. G51B–0433.

Cakir, Z., J.-B. Chabalier, R. Armijo, B. Meyer, A. Barka, and G. Peltzer (2003). Coseismic and early post-seismic slip associated with the 1999 Izmit earthquake (Turkey), from SAR interferometry and tectonic field observations, *Geophysical Journal International*, **155**, 1, p. 93–110.

Duffy, G. P., and J. E. Hughes-Clarke (2005). Application of spatial cross correlation to detection of migration of submarine sand dunes, *Journal of Geophysical Research*, **110**, F04S12, p. 1–11.

Fialko, Y. (2004). Probing the mechanical properties of seismically active crust with space geodesy: Study of the coseismic deformation due to the 1992 Mw7.3 Landers (southern California) earthquake, *Journal of Geophysical Research*, **109**, B03307

Fialko, Y., D. Sandwell, M. Simons, and P. Rosen (2005). Three-dimensional deformation caused by the Bam, Iran, earthquake and the origin of shallow slip deficit, *Nature*, **435**, 7040, p. 295–299.

Fialko, Y., M. Simons, and D. Agnew (2001). The complete (3-D) surface displacement field in the epicentral area of the 1999 M7.1 Hector Mine earthquake, California, from space geodetic observations, *Geophysical Research Letters*, **28**, 16, p. 3063–3066.

Haeussler, P. J., D. P. Schartz, T. E. Dawson, H. D. Stenner, J. J. Lienkaemper, B. Sherrod, F. R. Cinti, P. Montone, P. A. Craw, A. J. Crone, and S. F. Personius (2004). Surface Rupture and Slip Distribution of the Denali and Totschunda Faults in the 3 November 2002 M 7.9 Earthquake, Alaska, *Bulletin of the Seismological Society of America*, **94**, 6B, p. S23–S52.

Hudnut, K. W., A. A. Borsa, C. Glennie, and J.-B. Minster (2002). High-resolution topography along surface rupture of the 16 October 1999 Hector Mine, California, earthquake from airborne laser swath mapping, *Bulletin of the Seismological Society of America*, **92**, 4, p. 1570–1576.

James, W. R. (1966). Fortran IV program using double Fourier series for surface fitting of irregularly spaced data, *Computer Contributions, Kansas State Geological Survey*, **5**,, p. 1–19.

Kääb, A., and M. Vollmer (2000). Surface geometry, thickness changes and flow fields on creeping mountain permafrost: automatic extraction by digital image analysis, *Permafrost and Periglacial Processes*, **11**,, p. 315–316.

Lin, A., G. Rao, D. Jia, XiaojunWu, B. Yan, and Z. Ren (2011). Co-seismic strike-slip surface rupture and displacement produced by the 2010 MW 6.9 Yushu earthquake, China, and

implications for Tibetan tectonics, *Journal of Geodynamics*, **52**, 3-4, p. 249–259.

Lin, A., T. Ouchi, A. Chen, and T. Maruyama (2001). Co-seismic displacements, folding and shortening structures along the Chelungpu surface rupture zone occurred during the 1999 Chi-Chi (Taiwan) earthquake, *Tectonophysics*, **330**, 3-4, p. 225–244.

Lin, J., and R. S. Stein (2004). Stress triggering in thrust and subduction earthquakes and stress interaction between the southern San Andreas and nearby thrust and strike-slip faults, *Journal of Geophysical Research*, **109**, B02303

Michel, R., and J.-P. Avouac (2006). Coseismic surface deformation from air photos: the Kickapoo step over in the 1992 Landers rupture, *Journal of Geophysical Research*, **111**, B3, p. B03408.

Michel, R., and J.-P. Avouac (2002). Deformation due to the 17 August 1999 Izmit, Turkey, earthquake measured from SPOT images, *Journal of Geophysical Research*, **107**, B4, p. 1–6.

Michel, R., J.-P. Avouac, and J. Taboury (1999). Measuring ground displacements from SAR amplitude images: application to the Landers earthquake, *Geophysical Research Letters*, **26**, 7, p. 875–878.

Ozawa, S., M. Kaidzu, M. Murakami, T. Imakiire, and T. Hatanaka (2004). Coseismic and postseismic crustal deformation after the M8 Tokachi-oki earthquake in Japan, *Earth, Planets and Space*, **56**, 7, p. 675–680.

Phillips, D. A., M. E. Jackson, and C. Meertens (2008). GeoEarthScope Airborne LiDAR and Satellite InSAR Imagery, *Eos Trans. AGU*, **89**, 53, p. G53A–0630.

Prentice, C. S., C. J. Crosby, D. J. Harding, R. A. Haugerud, D. J. Merrits, T. W. Gardner, R. D.

Koehler, and J. N. Baldwin (2003). Northern California LIDAR Data: A Tool for Mapping the San Andreas Fault and Pleistocene Marine Terraces in Heavily Vegetated Terrain, *Eos Trans. AGU*, **84**, 46, p. G12A–06.

Pucci, S., N. Palyvos, C. Zabci, D. Pantosti, and M. Barchi (2006). Coseismic ruptures and tectonic landforms along the Düzce segment of the North Anatolian Fault Zone (Ms 7.1, November 1999), *Journal of Geophysical Research*, **111**, B06312.

Rabine, D. L., J. L. Bufton, and C. R. Vaughn (1996). Development and Test of a Raster Scanning Laser Altimeter for High Resolution Airborne Measurements of Topography, *in* IGARSS '96: 1996 International Geoscience and Remote Sensing Symposium, Lincoln, NE, p. 423–426.

Sandwell, D. T., L. Sichoix, and B. Smith (2002). The 1999 Hector Mine Earthquake, Southern California: Vector Near-Field Displacements from ERS InSAR, *Bulletin of the Seismological Society of America*, **92**, 4, p. 1341–1354.

Simons, M., Y. Fialko, and L. Rivera (2002). Coseismic deformation from the 1999 Mw 7.1 Hector Mine, California, earthquake as inferred from InSAR and GPS observations, *Bulletin of the Seismological Society of America*, **92**, 4, p. 1390–1402.

Slatton, K. C., W. E. Carter, R. L. Shrestha, and W. Dietrich (2007). Airborne Laser Swath Mapping: Achieving the resolution and accuracy required for geosurficial research, *Geophysical Research Letters*, **34**, L23S10, p. 1–5.

Toda, S., R. S. Stein, K. Richards-Dinger, and S. B. Bozkurt (2005). Forecasting the evolution of seismicity in southern California: Animations built on earthquake stress transfer, *Journal of Geophysical Research*, **110**, B05S16.

Treiman, J. A., K. J. Kendrick, W. A. Bryant, T. K. Rockwell, and S. F. McGill (2002). Primary surface rupture associated with the Mw 71. 16 October 1999 Hector Mine earthquake, San Bernadino County, California, *Bulletin of the Seismological Society of America*, **92**, 4, p. 1171–1191.

Trucco, E., A. Fusiello, and R. Vito (1999). Robust motion and correspondence of noisy 3-D point sets with missing data, *Pattern Recognition Letters*, **20**, p. 889–898.

Wdowinski, S., Y. Bock, J. Zhang, P. Fang, and J. Genrich (1997). Southern California Permanent GPS Geodetic Array: Spatial filtering of daily positions for estimating coseismic and postseismic displacements induced by the 1992 Landers earthquake, *Journal of Geophysical Research*, **102**, B8, p. 18057–18070.

Yun, S.-H., H. Zebker, P. Segall, A. Hooper, and M. Poland (2007). Interferogram formation in the presence of complex and large deformation, *Geophysical Research Letters*, **34**, L12305, p. 1–6.

Zielke, O., J. R. Arrowsmith, L. G. Ludwig, and S. O. Akciz (2010). Slip in the 1857 and Earlier Large Earthquakes Along the Carrizo Plain, San Andreas Fault, *Science*, **327**,, p. 1119–1122.

Authors' affiliations, addresses

Adrian Borsa

Scripps Institution of Oceanography

University of California, San Diego

9500 Gilman Drive #0225

La Jolla, CA 92093-0225

aborsa@ucsd.edu

Jean-Bernard Minster

Scripps Institution of Oceanography

University of California, San Diego

9500 Gilman Drive #0225

La Jolla, CA 92093-0225

jbminster@ucsd.edu

Tables

Table 1. Misfit statistics for selected displacement field solutions discussed in the text.

Pixel Size	15 meters	15 meters	***15 meters***	15 meters	15 meters
Model Resolution	12.5 meters	12.5 meters	***12.5 meters***	12.5 meters	12.5 meters
Topography/Intensity Weighting	λ = 1.0	λ = 1.0	***λ = 1.0***	λ = 1.0	λ = 1.0
Point Density	2 / m^2	2 / m^2	***2 / m^2***	2 / m^2	2 / m^2
Azimuth (Control Region)					
median misfit [deg]	-1.5	-0.5	***7.7***	11.4	0.8
misfit IQR (Interquartile Range) [deg]	181.5	176.4	***171.9***	175.5	178.9
Azimuth (Slipped Region)					
median misfit [deg]	0.0	0.0	***0.1***	0.0	0.1
misfit IQR [deg]	1.9	4.3	***1.4***	2.2	1.8
Horizontal Displacement (Control)					
median misfit [cm]	18.5	39.3	***10.1***	18.0	17.7
misfit IQR [cm]	17.9	36.7	***9.6***	18.0	16.6
Horizontal Displacement (Slipped)					
median misfit [cm]	17.1	35.0	***11.2***	18.4	14.6
misfit IQR [cm]	17.7	36.7	***12.9***	18.2	15.7
Vertical Displacement (Control)					
median misfit [cm]	0.6	1.3	***0.4***	0.6	0.7
misfit IQR [cm]	0.9	1.8	***0.5***	0.9	0.8
Vertical Displacement (Slipped)					
median misfit [cm]	0.5	1.2	***0.4***	0.6	0.6
misfit IQR [cm]	0.7	1.7	***0.6***	0.8	0.7

Note: the third column (in bold italic) shows results for the solution with the lowest overall misfit relative to the *a priori* imposed slip.

Figure Captions

Figure 1. Spatial resolution and spatial coverage of estimates of coseismic surface deformation/slip obtained using various techniques. Spatial resolution refers to the average distance between individual measurements, and spatial coverage indicates the areal extent of the measurements expressed as perpendicular distance from the fault trace (the ideal technique would yield high-resolution estimates from directly on the fault into the far-field). The airborne LiDAR correlation technique discussed in this paper offers higher resolution than alternative methods, with excellent coverage in the near-field of the fault.

Figure 2. (top) Aerial photo of our study area on the San Andreas Fault, 7 km northwest of Desert Hot Springs, CA. The thick rectangle shows the extent of the B4 Survey LiDAR data used in this study. Numerous erosion gullies and two roads are apparent, and vegetation is a sparse desert scrub. (bottom) Same as above, but showing shaded topographic relief generated from the LiDAR elevations. Not all the features in the photo are apparent in the topography, and vice versa.

Figure 3. (a) First-return LiDAR point cloud from the B4 Survey for a single pass over the study area in Figure 2, shaded for elevation. Topography is detrended to highlight surface features such as the N-S trending valley containing the main drainage channel, an E-W trending dirt road, and a SE-NW trending paved road. The line bisecting the point cloud separates synthetically-slipped points to the upper right from unslipped points to the lower left. (b) Same as (a), but with points shaded for LiDAR infrared backscatter intensity. The most obvious feature in the intensity image is the paved road, but other short-wavelength features are apparent as well.

Figure 4. Illustration of cross-correlation technique used in this paper. In Step A (top), the pre-event elevation point cloud is fit with a surface model H(x, y) consisting of 2-D harmonic basis

functions. In Step B (bottom), the post-event elevation point cloud within a pixel of size S is directly compared with H(x, y) and an iterative inversion is performed to solve for the single three-dimensional displacement vector x that minimizes the misfit between the point cloud and model for that pixel. In practice, point cloud intensities are also fit with a surface model and both topography and intensity are simultaneously inverted to yield x.

Figure 5. (a) The horizontal component of the 3D slip vectors obtained by applying the slip recovery algorithm to the data shown in Figure 3 using a pixel size of 15 m, fit resolution to "before" data of 12.5 m and equal weight between topography and intensity. Even without parameter tuning, the algorithm is generally successful at recovering the correct orientation and magnitude of the imposed synthetic slip, while indicating little or no slip in the control region. (b) Same as (a), but showing the vertical component of the recovered 3D slip. Vector magnitudes on the recovered slip plots are normalized to their maximum value, so the horizontal and vertical slip magnitudes cannot be compared directly between plots.

Figure 6. Horizontal slip recovered using the same inversion parameters and method as in Figure 5a, but initializing the algorithm with the magnitudes and orientations from the Figure 5a solution. The displacement field in the slipped region is much more uniform, reflecting the improvement due to starting the inversion for each pixel closer to the position of the misfit minimum. (b) Same as (a), but showing vertical slip recovered after initializing the algorithm with the slip from the Figure 5b solution.

Figure 7. Spatial plots (left) and summary histograms (right) of the misfit of the displacement solution shown in Figure 6. The spatial plots show that the recovered solution is faithful to the actual imposed slip, except directly on the boundary of the slipped and control regions. There are separate histograms for results from the control and slipped regions, which show that the

distribution of misfits clusters tightly around zero, except for the expected random distribution of azimuth misfit in the control region.

Figure 8. Median misfit of the displacement solutions for the slipped (top) and control (bottom) regions of the dataset. Dashed vertical lines group the misfit results by pixel size S, from 7.5 m to 15.0 m. The different shades within each pixel-size group represent stepwise changes in the resolution of the pre-event point cloud model, from 50.0 m (leftmost circles) to 25.0 m, 16.7 m, 12.5 m and 10.0 m (rightmost circles). Within each resolution grouping, the plotted points from left to right correspond to λ values of 0.0, 0.5, 1.0, 1.5, 2.0 and 2.5. The best overall solution we obtained in this experiment (see Table 1, column 3) had a pixel size of 15.0 m, model fit resolution of 10.0 m, and a λ of 1.5.

Figure 9. [Left] Recovered synthetic slip corresponding to modeled deformation from a 150-meter stepover between two right-lateral fault segments in our study area, each with 1 m total slip equally partitioned across the fault. The dashed lines in the vertical slip plot (bottom) indicate the locations of the faults. [Right] Histograms showing the misfit between the imposed synthetic slip and the estimated slip. The algorithm performed almost as well with this complex deformation pattern as it did with the simple uniform-slip case shown in Figure 6.

Figures

Figure 1.

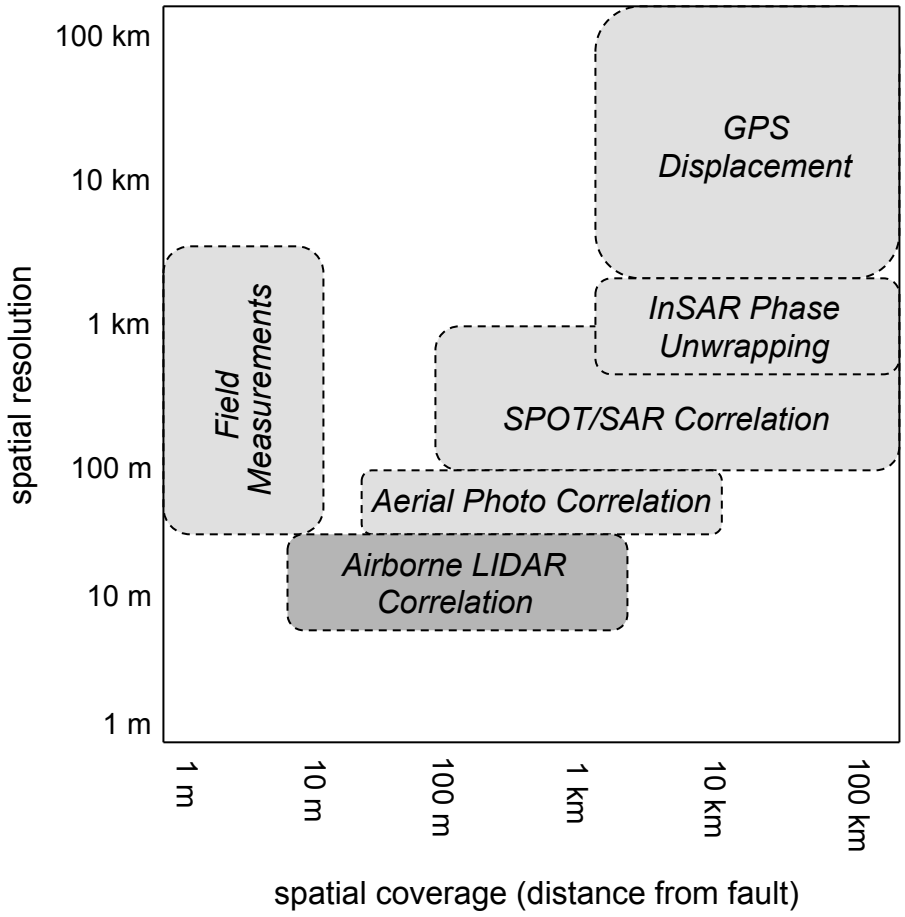

Figure 2.

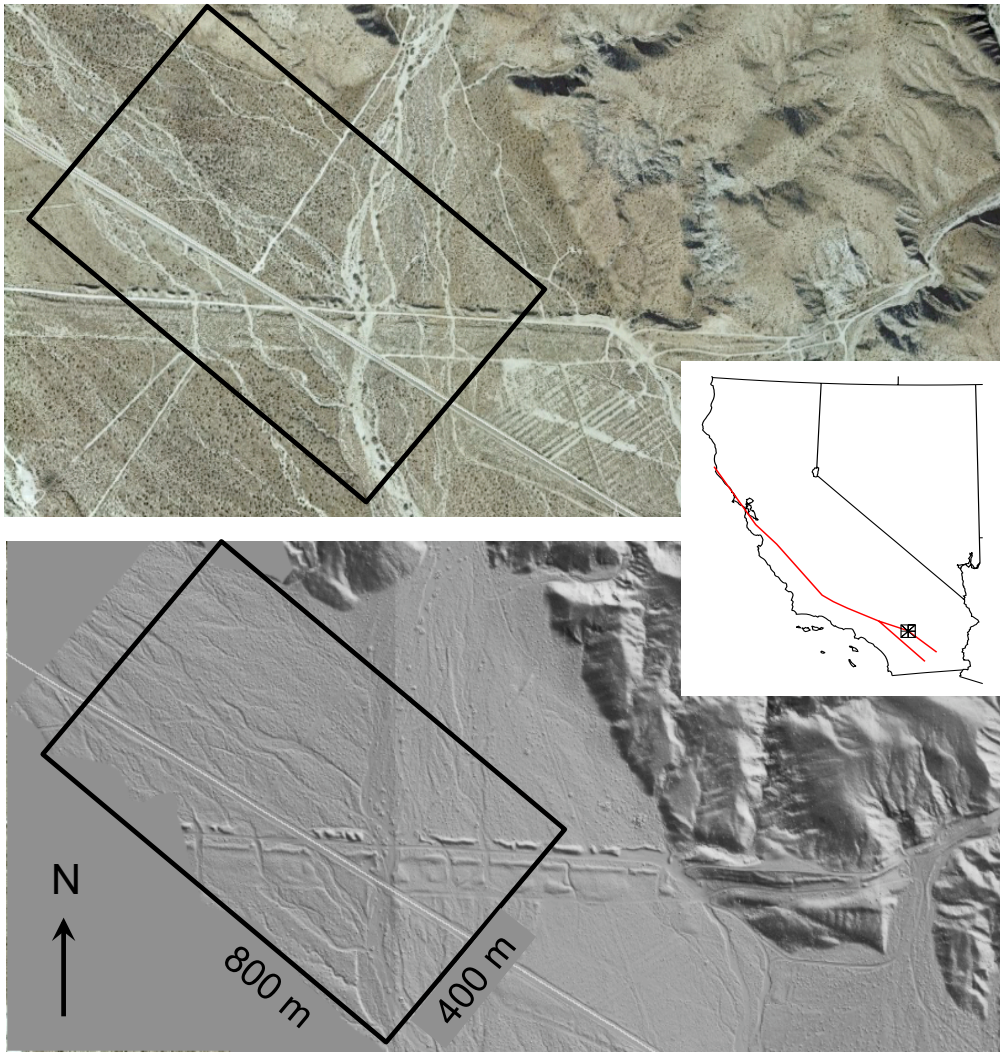

Figure 3a.

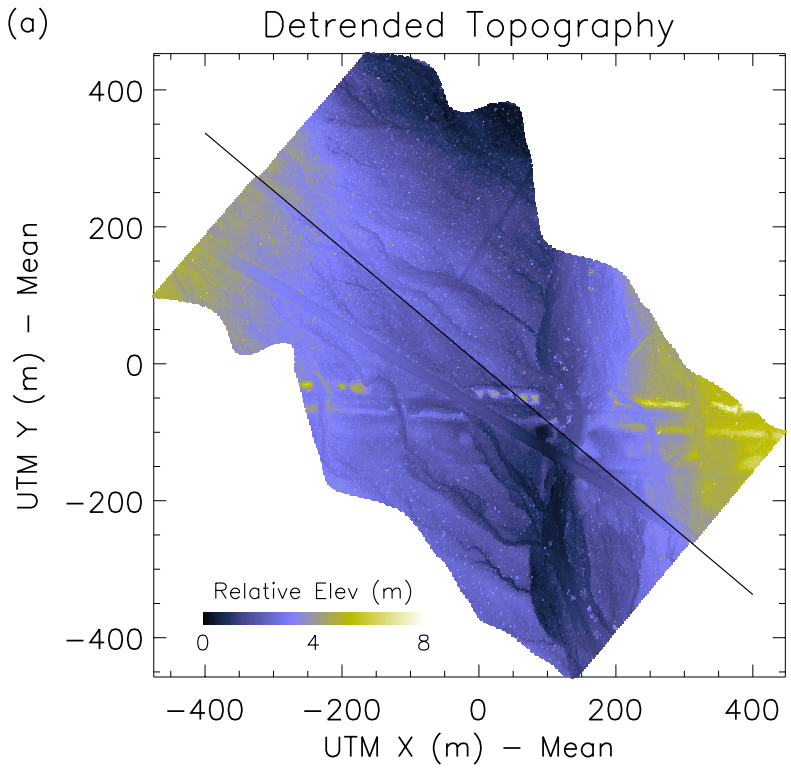

Figure 3b.

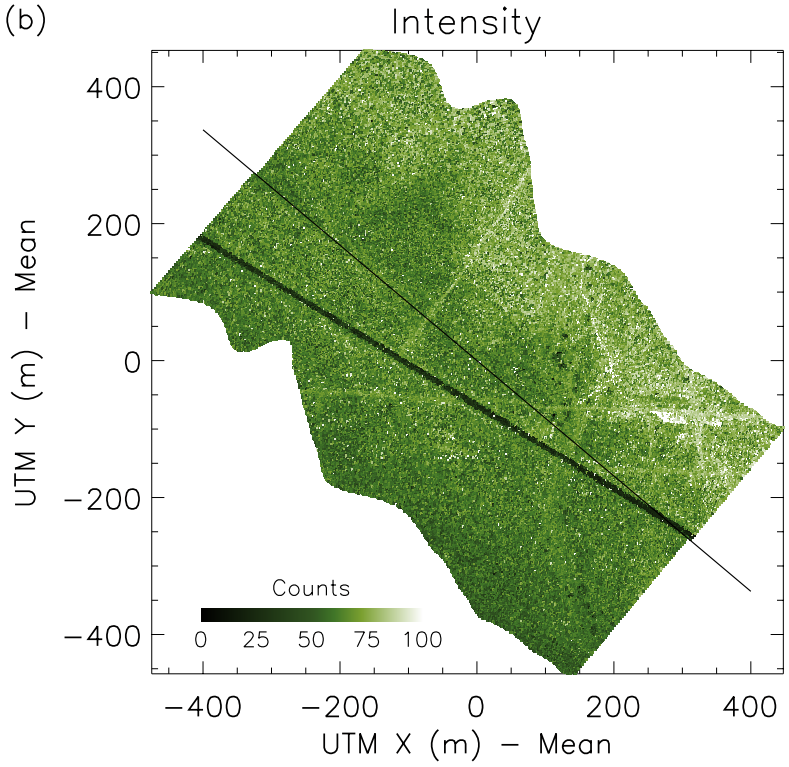

Figure 4.

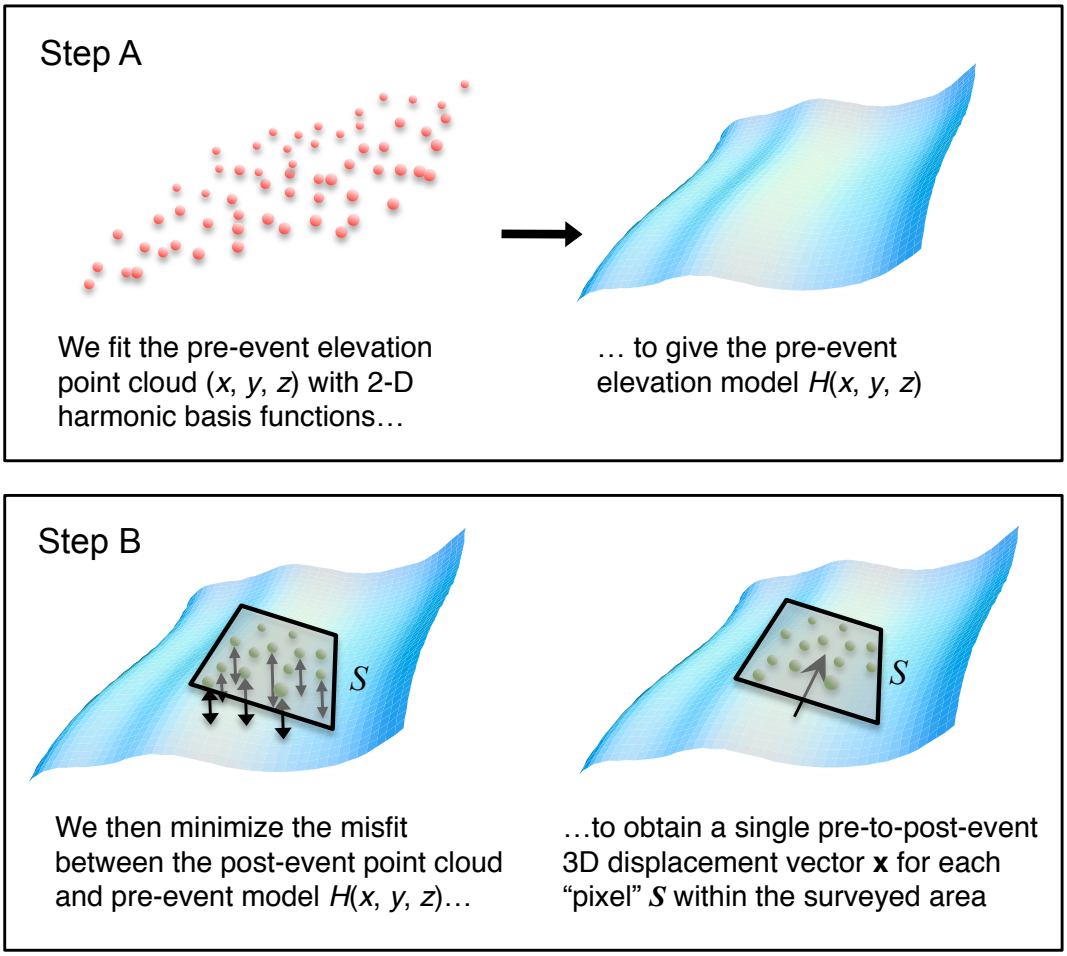
Step A
We fit the pre-event elevation point cloud (x, y, z) with 2-D harmonic basis functions…
… to give the pre-event elevation model H(x, y, z)
Step B
S
S
We then minimize the misfit between the post-event point cloud and pre-event model H(x, y, z)…
…to obtain a single pre-to-post-event 3D displacement vector x for each "pixel" S within the surveyed area

Figure 5a.

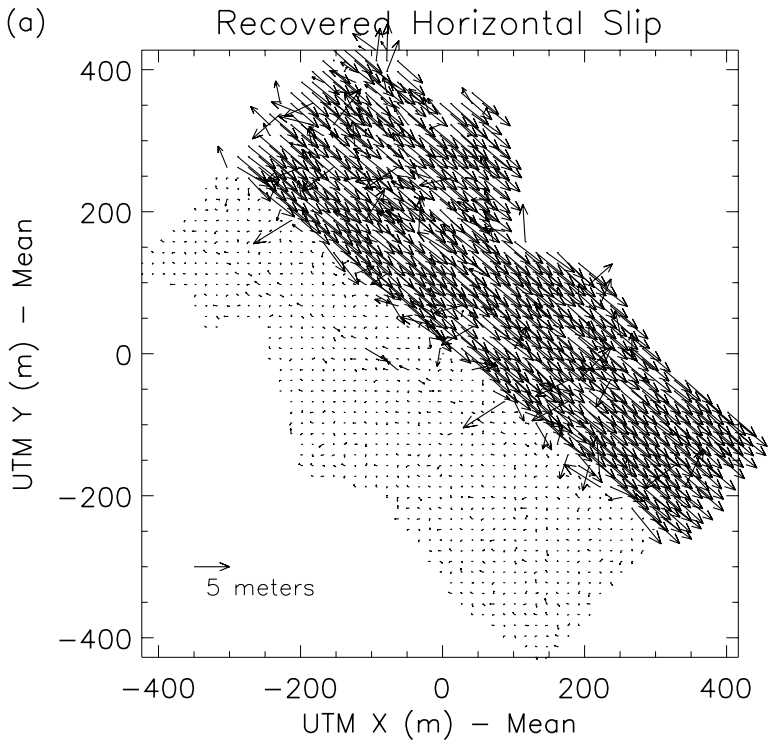

Figure 5b.

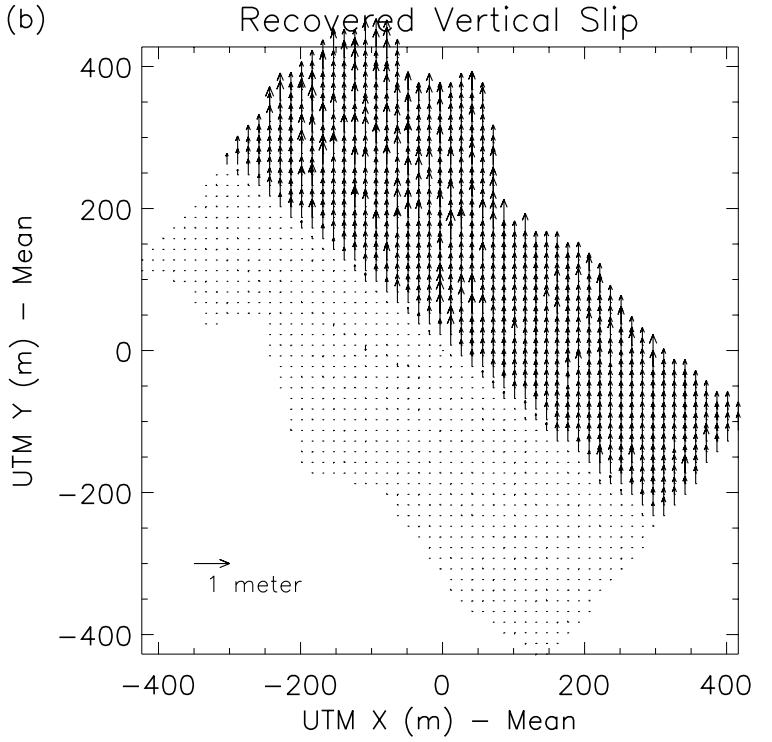

Figure 6a.

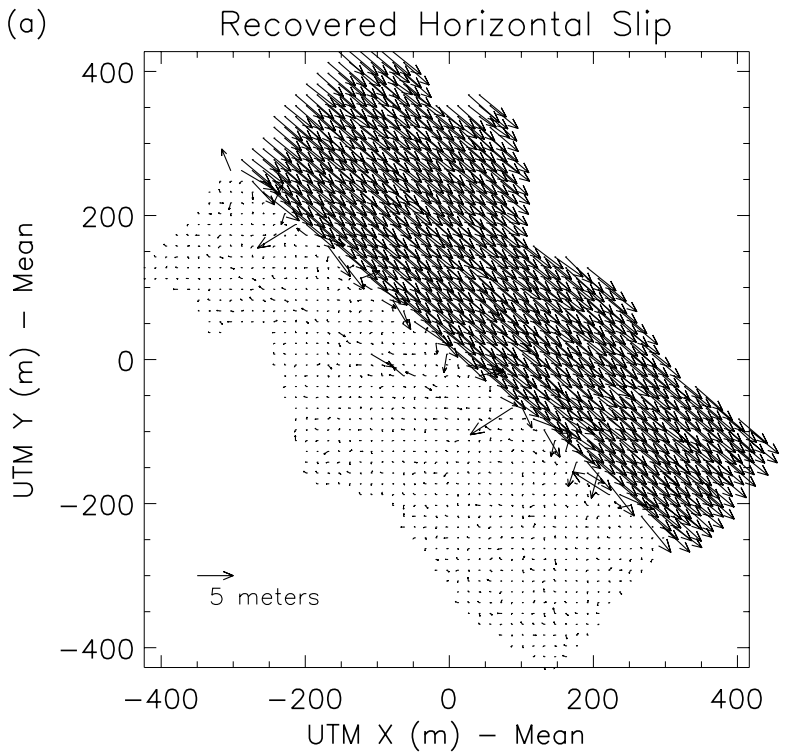

Figure 6b.

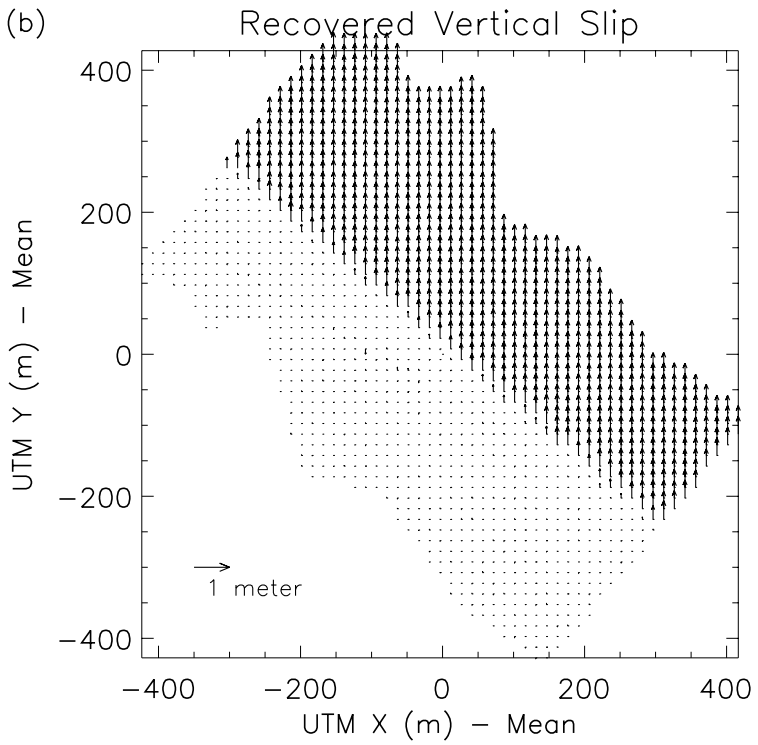

Figure 7.

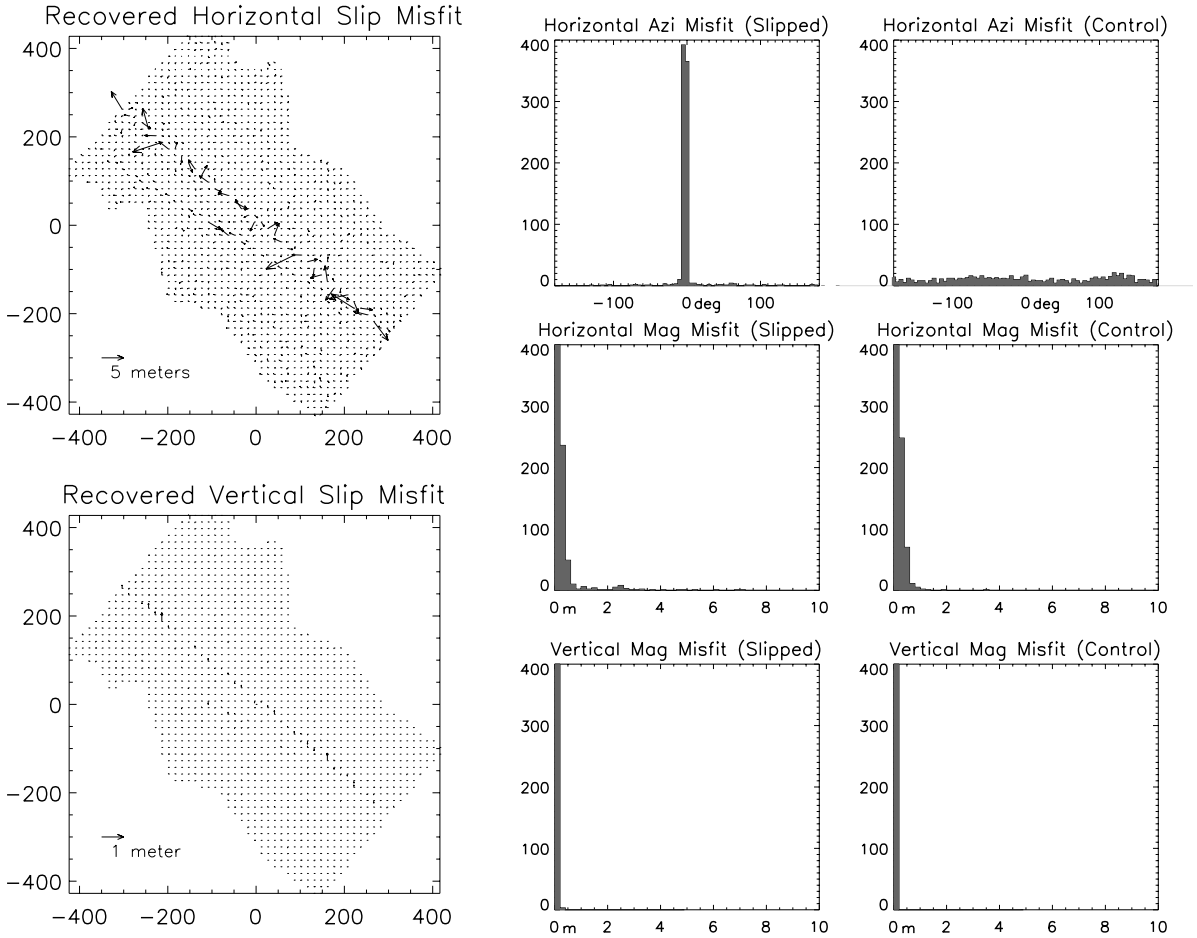
Recovered Horizontal Slip Misfit
5 meters
Recovered Vertical Slip Misfit
1 meter
Horizontal Azi Misfit (Slipped)
Horizontal Azi Misfit (Control)
Horizontal Mag Misfit (Slipped)
Horizontal Mag Misfit (Control)
Vertical Mag Misfit (Slipped)
Vertical Mag Misfit (Control)
0 deg
0 m

Figure 8.

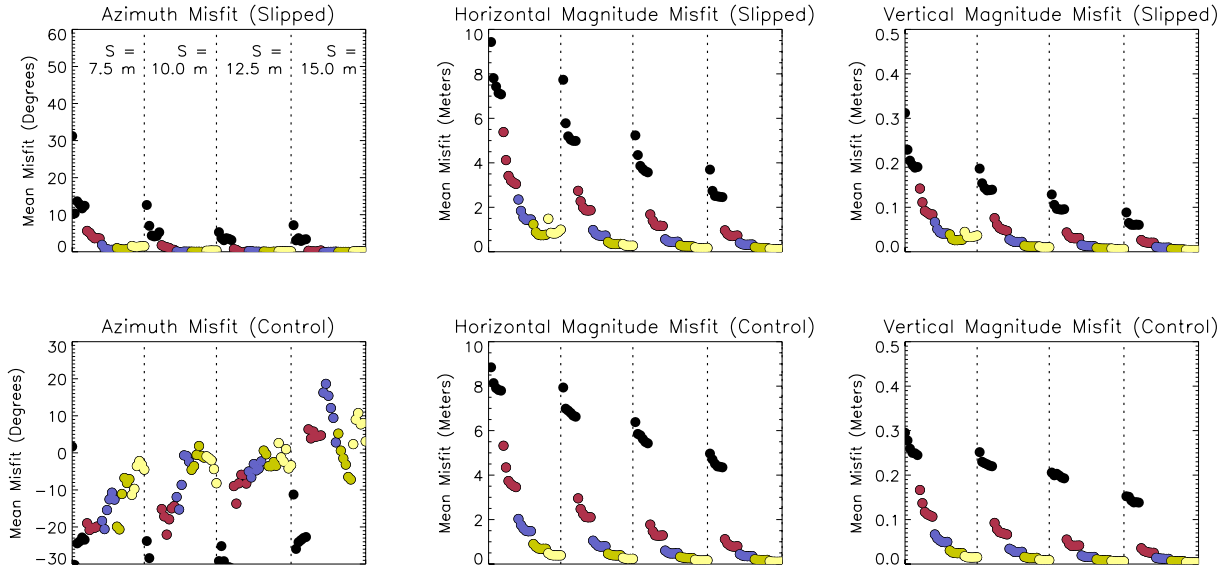
Azimuth Misfit (Slipped)
Horizontal Magnitude Misfit (Slipped)
Vertical Magnitude Misfit (Slipped)
Azimuth Misfit (Control)
Horizontal Magnitude Misfit (Control)
Vertical Magnitude Misfit (Control)
Mean Misfit (Degrees)
Mean Misfit (Meters)
S = 7.5 m
S = 10.0 m
S = 12.5 m
S = 15.0 m

Figure 9.

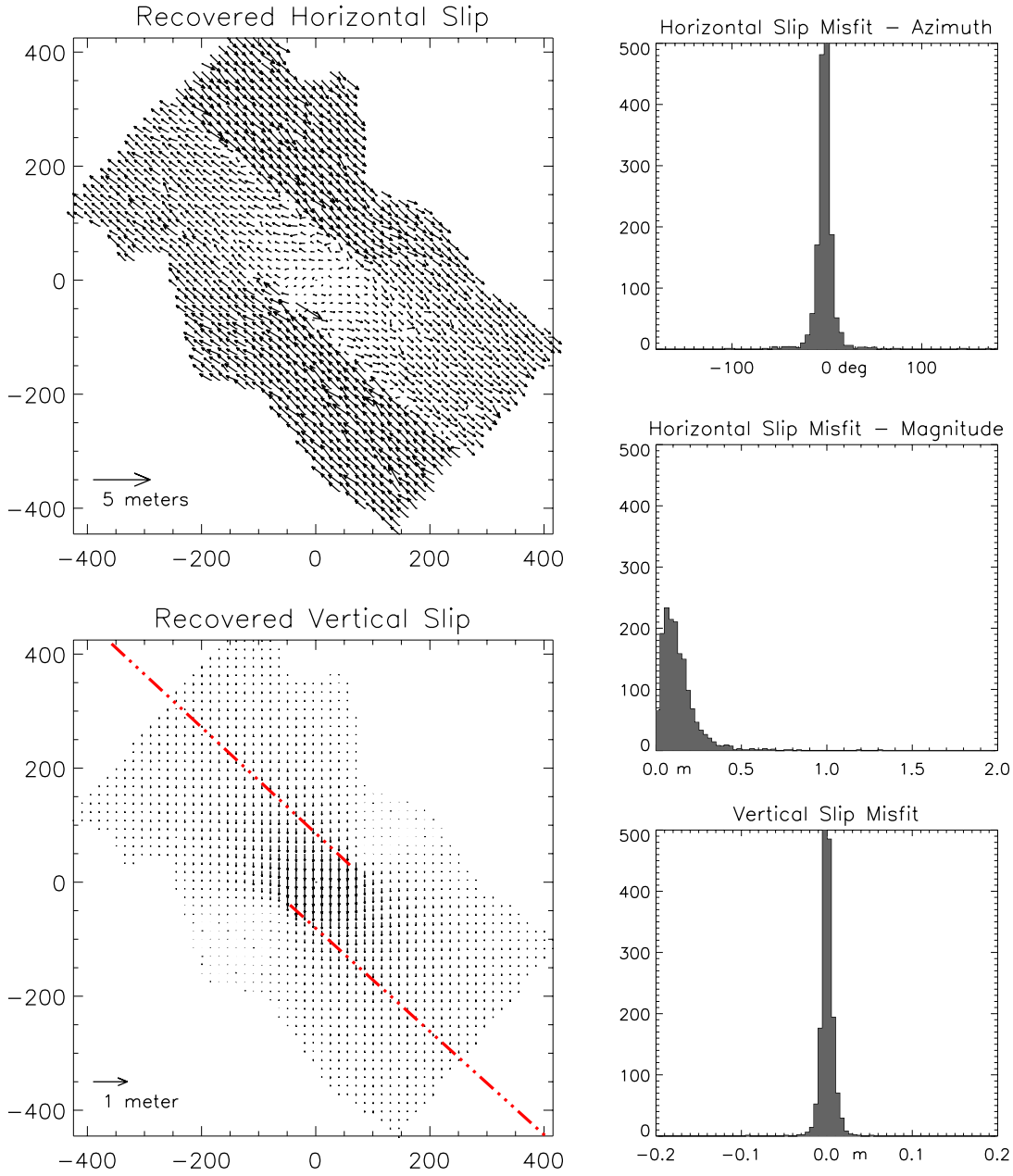
Recovered Horizontal Slip
400
200
0
−200
−400
5 meters
−400
−200
0
200
400
Horizontal Slip Misfit − Azimuth
500
400
300
200
100
0
−100
0 deg
100
Horizontal Slip Misfit − Magnitude
500
400
300
200
100
0
0.0 m
0.5
1.0
1.5
2.0
Recovered Vertical Slip
400
200
0
−200
−400
1 meter
−400
−200
0
200
400
Vertical Slip Misfit
500
400
300
200
100
0
−0.2
−0.1
0.0 m
0.1
0.2